Electron beam powder bed fusion of Ti–6Al–2Sn–4Zr–2Mo alloy: microstructure evolution and high-temperature mechanical properties

Progress in Additive Manufacturing
https://doi.org/10.1007/s40964-025-00996-8

FULL RESEARCH ARTICLE

Electron beam powder bed fusion of Ti–6Al–2Sn–4Zr–2Mo alloy: microstructure evolution and high-temperature mechanical properties

Abdollah Saboori[1,2] · Emanuele Tognoli[3] · Manuela Galati[1,2] · Lucia Denti[3]

Received: 4 June 2024 / Accepted: 21 January 2025

Abstract
Ti–6Al–2Sn–4Zr–2Mo (Ti6242) is a promising alloy for hot engine parts and gas turbine components, such as discs, impellers, and turbines, due to its excellent performance, particularly at high working temperatures. However, there has been limited research on its thermomechanical performance and microstructural evolution at high temperatures. This study aims to investigate the microstructural evolution and flow behaviour of this alloy produced via the electron beam powder bed fusion process. The plastic response in a temperature range of 25–620 °C was investigated using warm tensile tests under a constant strain rate. The outcomes showed that the plastic deformation capacity of the alloy extends significantly by increasing the temperature due to the annihilation of the dislocation density and activation of pyramidal slip systems. Microstructural observations revealed that with increasing temperature, even if the initial size of the β-grains remained in the range of 30–60 µm, the width of α lath enlarged. In addition, it was found that with higher test temperatures, the lattice strain diminished, while the crystallite size increased, which affected the tensile strength of the material. Analysis of the fracture surface revealed a mixed fracture mode of ductile and brittle nature at room temperature, while a completely ductile fracture was obtained at high temperatures. All in all, it can be concluded that among the materials produced by electron beam powder bed fusion, the mechanical performance of Ti6242 alloy can surpass that of Ti-6Al-4 V(Ti64) in the temperature range studied and is also superior to the same Ti6242 alloy produced by casting. This work paves the way for the replacement of the widely used Ti64 or heavier alloys, particularly for highly loaded parts at high temperatures.

Keywords Additive manufacturing · Electron beam powder bed fusion · Titanium · Ti6242 · Working temperature

1 Introduction

Over the past years, the development of titanium alloys has attracted great interest in various industrial sectors [1]. This attractiveness is due to their inherent properties, making them a promising candidate when it comes to weight reduction, improvement of overall performance, and mechanical and thermal properties of high-quality parts at high temperatures [2]. To meet these requirements, a series of near α-titanium alloys have been developed over the last years. Near α-titanium alloys have indeed shown unique properties, such as high specific strength, good high temperature characteristics, and excellent corrosion resistance up to 600 °C [3]. IMI834 (Ti–5.8Al-4.0Sn–3.5Zr–0.7Nb–0.5Mo–0.35Si–0.06C) [4], Ti1100 (Ti–6Al–2.75Sn–4Zr–0.4Mo–0.45Si) [5], BT36 (Ti–6.2Al–2Sn–3.6Zr–0.7Mo–0.15Si) [6], Ti60 (Ti–6Al–2.8Sn–4Zr0.5–Mo0.4–Si) [7], and Ti6242 (Ti–6Al–2Sn–4Zr–2Mo) [8] are the best known near α titanium alloys that have been used for the production of compressor discs and gas turbine blades for jet engines. Among them, Ti6242, a high-resistance near-α titanium alloy, exhibits high tensile strength and toughness and excellent resistance to creep, fatigue, and corrosion [9, 10]. In this alloy, several α stabiliser elements, such as Al, Sn, and Zr, are added together with a certain amount of Si

✉ Abdollah Saboori
abdollah.saboori@polito.it

[1] Department of Management and Production Engineering, Politecnico di Torino, Corso Duca Degli Abruzzi 24, 10129 Turin, Italy

[2] Integrated Additive Manufacturing Center (IAM@PoliTo), Politecnico di Torino, Corso Castelfidardo 51, 10129 Turin, Italy

[3] Department of Engineering "Enzo Ferrari", Università degli studi di Modena E Reggio Emilia, Modena, Italy

Published online: 14 February 2025

to increase the heat resistance and creep properties of the material [11, 12]. Hence, Ti6242 is well suited for high working temperatures, up to values ranging from 538 °C [13] to 550 °C [14] for the cast Ti6242. This exceptional behaviour makes the manufacturing of this material challenging using the conventional processes [15]. In addition, the scarce availability of the material, the low productivity, as well as the high production costs limit its usage in practical applications. For instance, it is reported that during the fabrication of the Boeing 787 airframe, which involves several machining steps, about 83% of the raw titanium alloy was wasted as machining chip [16]. Therefore, the adoption of Ti6242 is strictly limited to high-value components for the hottest sections of aerospace and racing engines [13, 17]. Thus, to broaden the application of this alloy in various fields, several investigations are being conducted to explore its processability by additive manufacturing (AM) techniques. In the case of laser powder bed fusion (*L*-PBF), the work was limited to investigating the processing conditions for producing fully dense and crack-free components [18]. For instance, Zhu et al. [19] investigated the mechanical performance of the *L*-PBF Ti6242 alloy under different heat treatment cycles. Rieger et al. [20] evaluated the high-temperature tensile properties of Ti6242 samples produced via the *L*-PBF process followed by machining at 500 °C. Their outcomes agreed well with the as-cast tensile properties. It was reported that a stress-relieving heat treatment should be performed to reduce the internal stresses in the as-built *L*-PBF Ti6242 samples and consequently increase their ductility. In the case of the electron beam powder bed fusion (EB-PBF) process, a modified Ti6424 alloy with boron was investigated by Fujieda et al. [21] and Cui et al. [22]. Lopez et al. [8] manufactured Ti6242 specimens via EB-PBF and tuned the tensile properties using different cycles of hot isostatic pressing (HIP). They reported a reduction of the residual defects and a concurrent increase in elongation by up to 15%. Recently, Galati et al. [10] demonstrated that it is possible to produce a fully dense (~99.9%) Ti6242 component by EB-PBF whose mechanical properties in the as-built condition at room temperature are comparable to those of the corresponding material in the as-cast condition. Although these results are promising, they do not cover performance at high temperatures, where alloy Ti6242 finds its preferred application. In fact, this alloy has been developed for high-temperature applications as an alternative of Ti-64 alloy, but its microstructural evolution and mechanical properties for the parts produced via EB-PBF process at high temperatures are missing in the literature. Hence, this work, for the first time, proposes an investigation of the microstructural evolution and mechanical properties of EB-PBF Ti6242 in a temperature range that exceeds the standard working conditions of the corresponding cast material. For this purpose, tensile tests were performed at 25 °C, 300 °C, 550 °C, and 620 °C at a constant strain rate. The results were analysed by seeking a correlation between the mechanical properties and the microstructural changes at elevated temperatures.

2 Materials and methods

2.1 Specimen production

The pre-alloyed Ti6242 powder with a particle size range of 45–106 µm supplied by TLS Technik GmbH & Co. was used as the feedstock material (D10 = 52 µm, D50 = 68 µm, and D90 = 99 µm). The tensile specimens, designed according to UNI EN ISO 6892-1 (Fig. 1), were produced using an Arcam A2X EB-PBF system. Five replicas were produced and tested for each temperature. All specimens were fabricated in a single job with the longitudinal axis perpendicular to the build plate. The layer thickness and preheating temperature were set to 50 µm and 700 °C, respectively. The process parameters used for the production are reported in Table 1. After construction, the job was cooled inside the vacuum chamber under a helium atmosphere. The specimens were then blasted using the same raw powder to remove the adhering sintered particles. Prior to the tensile tests, the ends of the specimens were threaded M10 × 1.0 mm to fit the tensile machine.

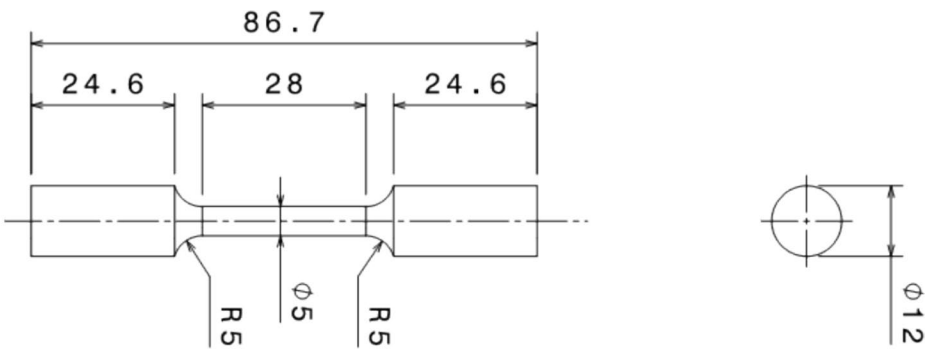

Fig. 1 The geometry of the as-built tensile specimens

Table 1 Process parameters used in this work for the sample production

FO [mA]	Speed [mm/s]	Speed function	LO [mm]	Reference current [mA]	Layer thickness [mm]
10	1060	− 176.7	0.2	10	0.050

Table 2 Temperature setting and duration of the tensile tests

T [°C]	T_{ramp} [°C/min]	Test duration [min]
25	–	5
300	10	45
550	18	55
620	18	64

2.2 Microstructure characterization

Microstructural analysis of the samples was performed using a Nikon SMZ1270 (Nikon, Tokyo, Japan) optical light microscope (OM) and a scanning electron microscope (SEM) ESEM Quanta 200 (FEI Company, Bruker Corporation, Hillsboro, Oregon, USA) after etching with Kroll's reagent (6.0 vol.% nitric acid and 3.0 vol.% hydrofluoric acid in water). For microstructural analysis, a piece of a tensile sample heat-treated at the temperatures used in the tensile tests was cut, mounted, and ground to #2400 grit. The samples were then polished down to 1 µm following the standard procedure reported for a Ti-6Al-4 V alloy [22]. The phase analysis of the samples has been conducted using *X*-ray diffraction (XRD) test with Cu K_α radiation ($\lambda = 1.54$ Å) operated at 40 kV and 40 mA with a step size of 0.02° and a counting time of 1 s per step, 2theta from 20 to 80 degree.

2.3 High-temperature tensile tests

Room- and high-temperature tensile tests were performed according to the standards UNI EN ISO 6892-1 and UNI EN ISO6892-2 using a Zwick Roell Z050 machine. 10 MPa was applied as preload, while 25 °C (room temperature), 300 °C, 550 °C, and 620 °C were used as test temperatures. Three thermocouples were placed along the specimen gauge length and were used to monitor that, during the test, the temperature remained uniform on the specimen and fixed at the nominal value, with a maximum deviation of ± 3 °C. The temperature ramp was slower for the tests at 300 °C to ensure comparable overall duration across the tests (Table 2). Once the set temperature was reached, it was maintained for 10 min before starting the tensile tests to guarantee a homogeneous temperature distribution. The strain was measured using a single-camera optical strain transducer with a gauge length of 25 mm. The tests were conducted under the control of a strain rate that was kept constant at $(2.5 \times 10^{-4} \pm 0.5 \times 10^{-4})$ s^{-1}.

3 Results and discussion

3.1 Microstructure analysis

A microstructural investigation was carried out to complement the study of the mechanical behaviour of Ti6242 at different temperatures. It is widely acknowledged that metal AM processes are characterized by extremely rapid solidification, resulting in the formation of different as-built microstructures compared to conventionally manufactured ones. Indeed, the fast and directional solidification during the EB-PBF process determines the morphology and size of the local microstructure, specifically resulting in extremely fine grains, preferential crystallographic orientation, and anisotropy in the mechanical properties. Figure 2a, b shows the OM, and Fig. 2c, d SEM images of the as-built microstructure of the Ti6242 tensile sample. The build direction (BD) is vertical and indicated in the micrographs. No cracks or macro-porosity were detected in the as-built samples, confirming the successful processing of this alloy via the EB-PBF. The porosity evaluation through the CT scan analysis as well as Archimedes method, which have been presented in our previous work, revealed that the relative density of the as-built samples was as high as 99.7% [10]. Moreover, the microstructure did not show any chemical inhomogeneity, normally leading to layered bands forming. On the other hand, Fig. 2a confirms the epitaxial grain growth along the steep temperature gradient in the build-up direction, leading to the formation of columnar β-grains with an average width of 30–60 µm. This size of columnar grains is the result of the permanence time of the material at the temperatures between the liquidus and β-transus temperatures of the Ti6242 alloy. It is also well documented that several factors, including the overheating of the molten pool, a narrow liquid/solid phase range, a high thermal gradient, and heat dissipation along the build-up direction, contribute to the epitaxial growth of the prior β-grains [23]. Since the EB-PBF process is characterized by rapid solidification, the formation of non-equilibrium phases, such as the hexagonally packed acicular martensite phase (α') in the as-built Ti6242 alloy, is expected. The Primary driving force for the α' phase formation is the reduction in free energy. The α' martensitic phase is a product of a diffusionless transformation of the β-phase into the low-temperature α-phase. Nevertheless, in this case, a preliminary Widmanstätten microstructure with basket-weave morphology and α-colonies was observed within the prior β-grains (Fig. 2b). The absence of α' in the as-built

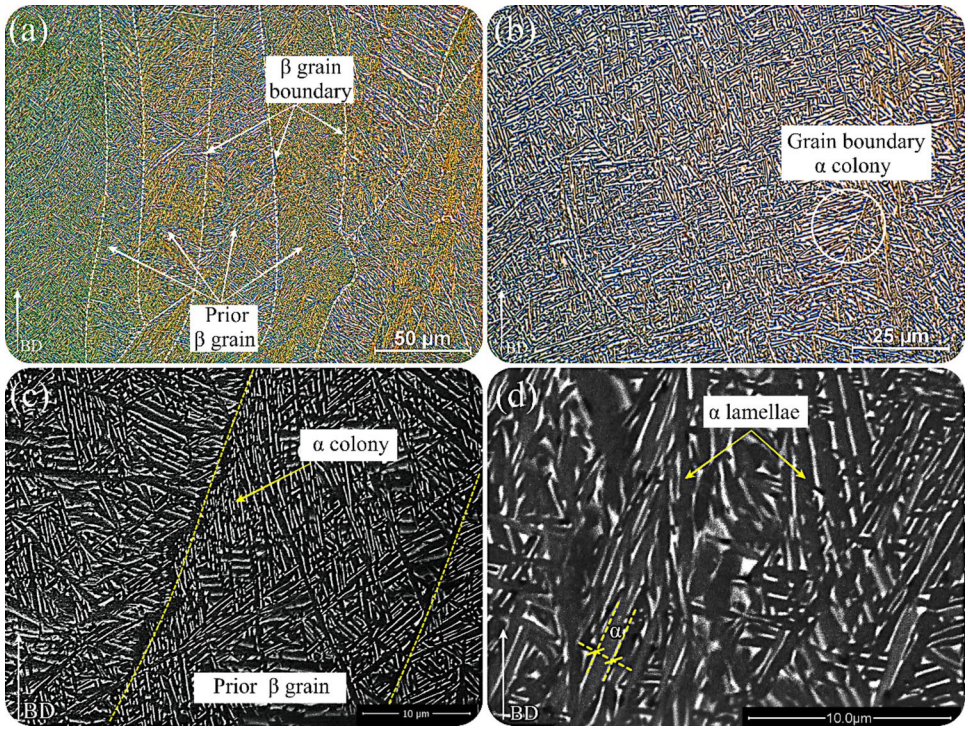

Fig. 2 **a-b** OM and **c-d** SEM micrograph of the as-built Ti6242 alloy

state may be related to the thermal history during the EB-PBF process, which provides a suitable condition for the decomposition of α'-martensite into α and β. On the other hand, it is well documented that Mo as a β stabiliser alloying element in Ti6242 reduces α-formation during phase transformation compared to the Ti64 alloy containing V. As a matter of fact, by decreasing the formation rate of α, the microstructure most likely consists of secondary α in the basket-weave structure. As can be seen in Fig. 2c, α-colonies nucleated from the prior β-grain boundaries with an approximate orientation of $\pm 45°$ to the grain boundary itself (yellow dashed lines). It is well documented that this arrangement is due to the Burgers orientation relationship between β and α during rapid solidification. Figure 2d shows an in-depth analysis of the as-built microstructure at high magnification using SEM. In this figure, the brighter regions are β phase enriched in heavy elements such as Mo, whereas the darker zones are α-laths enriched in α-stabiliser elements such as Al. In addition to the qualitative evaluation, a quantitative examination was also performed using the image analysis method to evaluate the α-lath thickness in the samples. The outcomes demonstrated that the average α-lath thickness in the as-built samples is 0.75 µm and the residual β-phase is distributed between the α-laths.

Figure 3 shows the OM microstructure of Ti6242 alloy after tensile testing at different temperatures. As can be seen in these micrographs, the general microstructure for all specimens comprises columnar grains grown in the direction of the maximum thermal gradient. In this work, the width of the columnar grains was measured using the line-intercept method. No significant growth of the prior β grain size was observed when the test temperature was increased. The average prior β grain width lies in the range of 30–60 µm, which corresponds to the range of as-built samples. The limitation of the growth of the prior β grain may be due to the presence of α phase in the microstructure of the samples in the sub-β transus region (995 °C). Another important microstructural feature that affects the mechanical properties of Ti6242 alloy is α lamellar thickness, where a fine α-lath thickness can promote good strength and ductility in the alloy with lamellar microstructure. It is well reported that the α-lath thickness at elevated temperatures in the sub β-transus regions mainly depends on the temperature and isothermal time, whereas at the temperatures above, the β-transus cooling rate determines the α-lamella width [24].

Figure 4 shows the variation of the Ti6242 microstructure at high magnifications as a function of the test temperature. As can be seen in this figure, by increasing the working temperature, the width of α-lath increases from 0.75 µm in the as-built state to 0.92 µm, 1.11 µm, and 1.75 µm at 300 °C, 550 °C, and 620 °C, respectively (Table 3). The α-lath thickness can inversely affect the mechanical properties of the material, such that as the α-lath thickness increases, the mechanical strength of Ti6242 alloy decreases. This correlation between the mechanical strength and α-lath width is related to the space between two phases that influences the dislocation slip length. In fact, by increasing the α-lath thickness, the space between two phases increases, leading

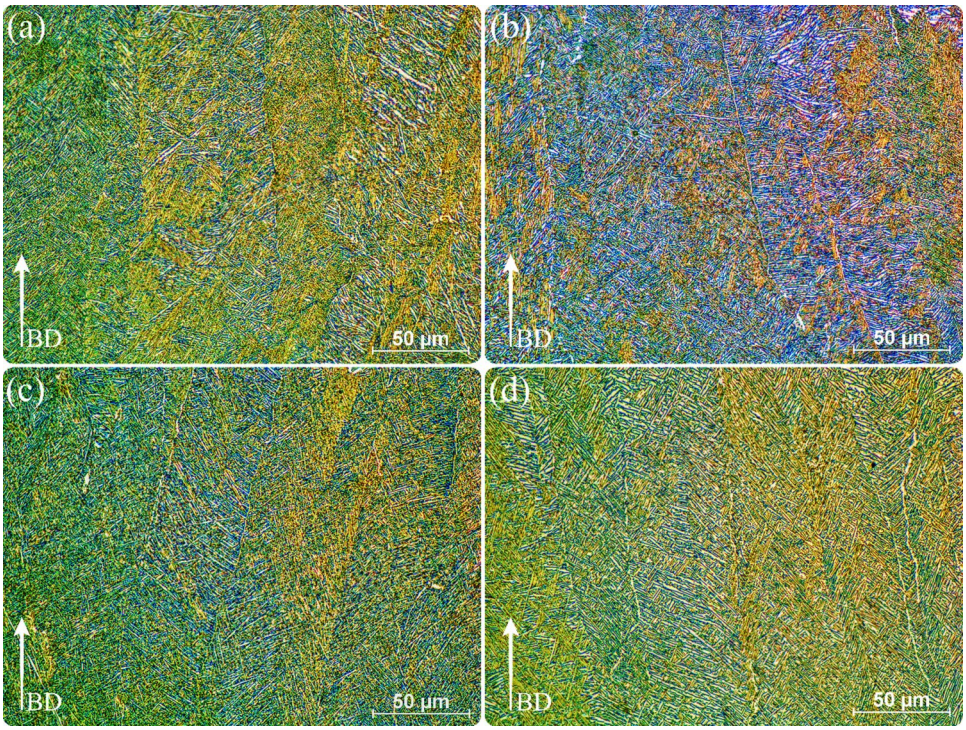

Fig. 3 OM micrographs of the Ti6242 alloy after tensile testing at different temperatures: **a** room temperature, **b** 300 °C, **c** 550 °C, and **d** 620 °C

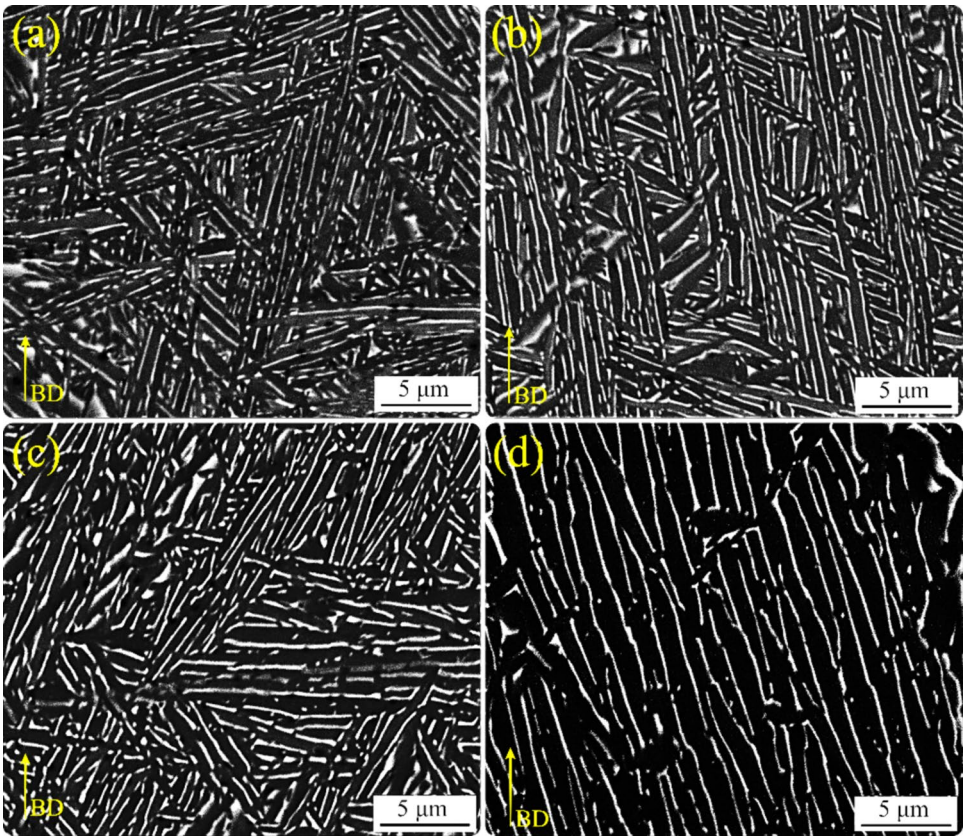

Fig. 4 SEM micrographs of the Ti6242 alloy tested at different temperatures; **a** room temperature, **b** 300 °C, **c** 550 °C, and **d** 620 °C

Table 3 The width of α-lath as a function of temperature

Temperature	25 °C	300 °C	550 °C	620 °C
α-lath thickness	0.75 ± 0.15	0.92 ± 0.11	1.11 ± 0.09	1.75 ± 0.14

to a higher dislocation slip length and, consequently, lower mechanical strength. On the other hand, it can be concluded that fine α-lath thickness can improve the mechanical properties of materials through the Hall–Petch strengthening mechanism and enhance its durability via higher strain accommodations that can increase the crack propagation resistance.

On the other hand, it is very interesting to highlight that the microstructure of the as-built Ti6242 alloy produced via the EBM process was finer than its counterpart Ti64 reported in the literature [25]. Figure 4a shows that the α lath thickness is in the range of 0.47–0.88 µm in the as-built condition, whereas in the case of as-built Ti64, it is in the range of 1–2 µm [25]. This discrepancy can be attributed to the chemical composition of these two alloys and the role of the individual alloying elements. Mo in the Ti6242 alloy, as one of the main alloying elements, has a very slow solid-state diffusivity compared to V in Ti64, which has the slowest solid-state diffusivity in this alloy [26]. This difference in the solid-state diffusivity of these alloying elements may hinder the growth rate of the α laths during the phase transformation from β to α [27]. It is well documented that boundary mobility can be controlled through a drag pressure that a solute like Mo can exert. This drag pressure depends strongly on the degree of grain boundary segregation and solid-state diffusivity of the solute and can be theoretically modelled by the Cahn–Lücke–Stüve impurity-drag model [28]. Since Ti64 and Ti6242 alloys experience nearly identical thermal histories during the EBM process, including multiple heating cycles, their microstructures have ample opportunity to grow. Therefore, as revealed in this work, the alloy with slower diffusing alloying elements such as Mo will be characterized by a finer microstructure that results in higher mechanical properties.

3.2 XRD phase analysis

XRD diffractograms of Ti6242 samples produced via the EB-PBF process and tested at high temperatures of 300, 550, and 620 °C were analysed over a wide 2θ range (25–90°) and compared with those of the material tested at room temperature (Fig. 5). As can be seen in Fig. 5a, unlike the Ti6242 alloy processed via the *L*-PBF process, which is characterized by a complete α/α' phase, the samples from EB-PBF exhibited duplex α with the hexagonal closed-packed (HCP) and β with a body-centred cubic (BCC) structure. This as-built phase composition originated from printing and in-situ

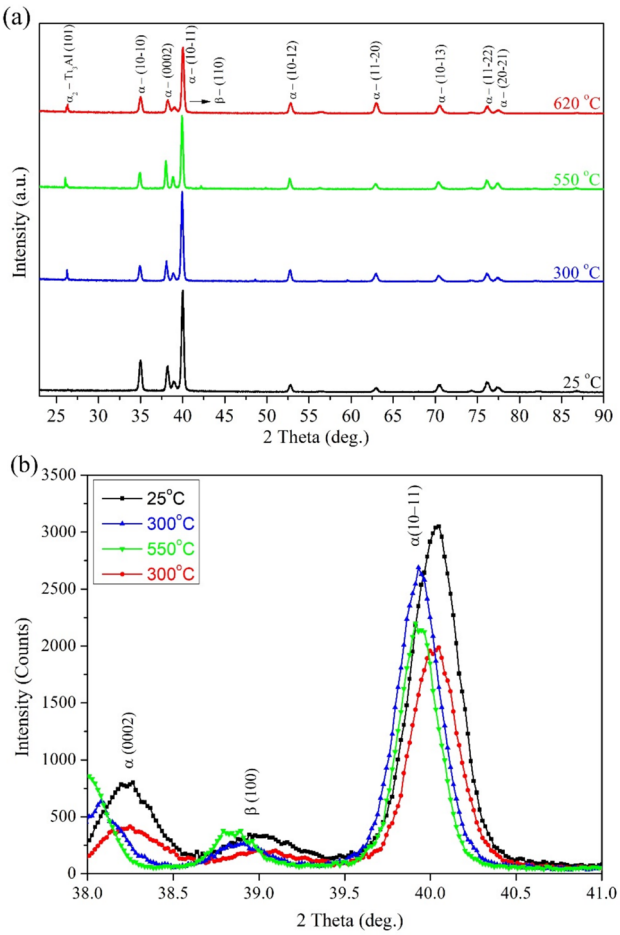

Fig. 5 **a** XRD plot of the Ti6242 samples tested at different temperatures and **b** magnified spectrum to show the emergence of β (110) peak

heat treatment of samples during the EB process. As a matter of fact, the rapid solidification during the ED-PBF process can result in the formation of metastable β phase which is not typically found in the conventional Ti6242 samples. This rapid solidification prevents the complete transformation of the β phase to the α phase during cooling. On the other hand, since EB-PBF process is a hot process, the condition for the diffusion of atoms is provided. Therefore, this unique chamber condition helps the decomposition of α' to a duplex α/β. It is evident that by increasing the test temperature from room temperature to 620 °C, the peak intensity of the α phase followed a decreasing trend, whereas that of the β phase remained almost unchanged. This variation implies that the relative content of the different phases changed due to the permanence at the test temperature for about 1 h, leading to an increase of the β phase fraction with increasing temperature.

In general, a higher α/β ratio results in higher mechanical strength and lower elongation owing to the different

intrinsic properties of the HCP and BCC phases. According to the thermodynamic calculations performed in the previous works, the formation of a certain amount of α_2-Ti_3Al phase and silicide can be expected in the α phase of Ti-xAl alloys ($x > 5$ wt.%) during the ageing treatment [20]. It is interesting to highlight that in this work, even if no peak associated with the α_2-Ti_3Al phase and silicide were found in the as-built Ti6242 samples when the test temperature was increased, a peak related to the α_2-Ti_3Al phase appeared at ~26°. The formation of this phase needs Al-rich zones that can originate from the diffusion processes facilitated at high temperatures [29, 30]. However, it should be noted that separating the α_2 from the α peaks is challenging at angles above 35° because of the very close diffraction positions [31]. Due to the nature of the EB-PBF process, which is a hot process, and the preheating temperature used in this work (700 °C), incipient local segregation of alloying elements, particularly Al, can be expected. Nevertheless, as reported earlier, no peak related to Ti_3Al was found in the XRD pattern of the as-built sample in this work. This discrepancy can be related to the rapid solidification of the EB-PBF process, which avoided the in-process segregation of Al, or, if it exists, limited the quantity of this phase below the XRD resolution. Köpper et al. [32] reported that the diffusion coefficient of Al in α-Ti was 2.17×10^{-21} m^2s^{-1} at about 660 °C, suggesting that, in this work, the preheating phase at 700 °C may act as a direct ageing treatment causing the precipitation of Ti_3Al phase. Li et al. [33] also found that the elemental diffusion at temperatures below 600 °C is slow and can be promoted at higher temperatures, resulting in a high local concentration of Al. The apparent inconsistency between literature predictions and experimental results could be solved by a deeper analysis through the Transmission electron Microscope (TEM) to confirm the absence of Ti_3Al. Moreover, contrary to the thermodynamic calculations concerning silicide precipitation, no peak associated with this phase was found. This contradiction in phase detection can be related to the silicide content, which might be lower than the resolution of the XRD analysis. For a precise comparison, the XRD patterns were plotted in the range $2\theta = 38–41°$ and then analysed from the α (10–11) peak using the X'Pert HighScore software and Scherrer calculator that determines crystallite size or lattice strain. The magnified spectrum of the XRD patterns shown in Fig. 5b points out that increasing the test temperature reduces the full width at half maximum (FWHM) of the α phase. This finding confirms that, by increasing the temperature, the crystallite size of samples increased, which is in line with the microstructural observations.

Moreover, a detailed analysis of Fig. 5b reveals that the peak positions of the samples shift to lower 2θ angles as the test temperature increases. This shift in peak positions can be attributed to diffusion processes and altered lattice structures according to Bragg's law ($2.d_{hkl}.\sin(\theta)) = n.\lambda$), [20]. Indeed, at high temperatures, Mo with a small atomic radius of 0.139 nm compared to the Ti atomic radius (0.147 nm) diffused from the interior to the grain boundary and precipitated the Mo-enriched phase [34]. Due to this precipitation, the Mo content in the α phase decreased, and consequently, the α peak shifted to lower 2θ angles. In addition to the peak shift, the effect of peak broadening is also observed, which results from the scattering of the d_{hkl} values. This peak broadening effect can be generally related to the instrumental effect, micro-stress in the crystallite or nano-size effects [18, 35]. Since in this work, all XRD analyses were performed under identical conditions for all the samples, the instrumental effect should be excluded. On the other hand, the nano-size effect is usually considered for nanocrystalline materials and cannot be considered as one of the influencing factors [36]. The last influencing factor is crystalline micro-stresses originating from crystal defects like lattice distortions. In general, solid solutions and dislocations have been reported as the main cause of these lattice distortions [18]. It is well documented that all samples underwent a rather complex thermal history during the EB-PBF process, which can result in a local inhomogeneity in the distribution of dislocations and solid solutions. As a consequence, slightly different micro-stresses can be generated and scatter the distribution of the d_{hkl} values. Figure 6 shows the variation of the lattice strain and crystallite size of the Ti6242 alloy as a function of the test temperature. As can be seen, the lattice strain decreased with increasing temperature, whereas the crystallite size increased. In addition, the variation of FWHM confirms that the dislocation density of Ti6242 samples reduced when the temperature increased from room temperature to 620 °C and consequently the lattice parameter changes.

3.3 Mechanical properties

The room-temperature tensile stress–strain curves of alloy Ti6242 produced by the EB-PBF process are illustrated in Fig. 7. The Ultimate Tensile Strength (UTS), Yield Strength (YS), and elongation at break (ε) of the as-built Ti6242 alloy are 914 ± 8 MPa, 853 ± 10 MPa, and 7.9 ± 0.9%, respectively. All five tensile curves agree perfectly, and no significant deviation was found.

Table 4 compares the mechanical properties of the as-built Ti6242 alloy processed in this work with those of the *L*-PBF and conventionally manufactured counterparts.

Table 4 shows that the strength of the as-built *L*-PBF Ti6242 alloys is higher than that processed by the EB-PBF process, while the elongation at break is inversely related. This discrepancy can be attributed to residual stress level, homogeneity in the chemical composition, oxygen and impurity pick-up, and the different microstructure and

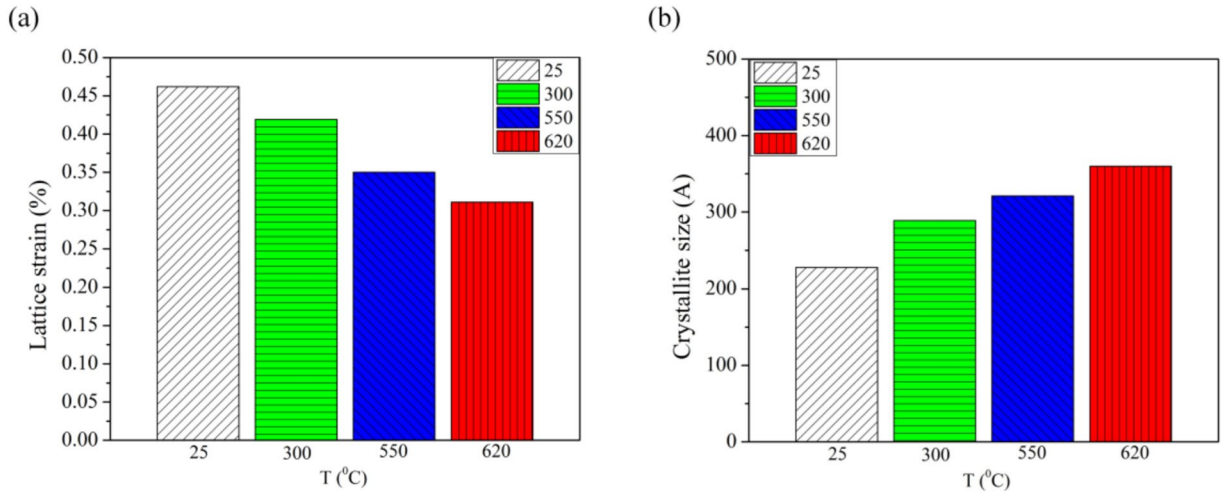

Fig. 6 **a** Lattice strain, and **b** crystallite size of the Ti6242 alloy tested at different temperatures

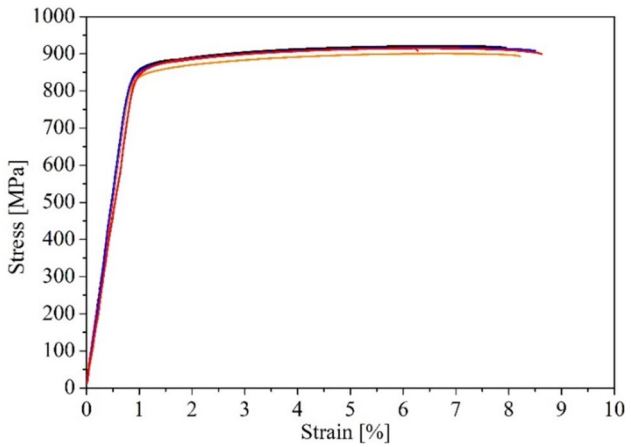

Fig. 7 Engineering tensile stress–strain curves of Ti6242 alloy at room temperature

phase compositions resulting from the two processes. It is well documented that the cooling rate in the *L*-PBF process is around 10^4–10^6 K/s, which is much faster than in the EB-PBF process [38]. Higher cooling rates lead to the formation of a finer microstructure consisting of slightly different phases in the *L*-PBF samples compared to EB-PBF. According to the Hall–Petch strengthening mechanism, a finer microstructure can improve the mechanical strength of the material. In the previous studies, the high solidification rate led to the formation of the non-equilibrium martensitic α' phase, comprising a high dislocation density, and also suppressed the precipitation of the β phase [18]. The low ductility of the *L*-PBF specimens in the as-built condition can be related to the formation of α'-martensite, which is characterized by little plastic deformation ability as well as higher levels of residual stresses compared to those of EB-PBF one. In general, according to AMS 4979G, alloy Ti6242 is commonly produced in the forged state [39]. On the other hand, it is found that the casting of Ti6242 parts is usually followed by an ageing step that could result in comparable performance to a part treated with an intermediate solid solution [37]. Surprisingly, the mechanical properties of the Ti6242 alloy processed in this work were similar to those obtained by casting and subsequent ageing treatment. Due to the nature of the EB-PBF process, which generally entails a more rapid solidification, and a finer microstructure as compared to casting methods, a higher mechanical strength can be expected. To find the reason for this unpredictably low tensile strength, the rupture surface of the samples was analysed. As can be seen in Fig. 8, high surface roughness and internal defects were prominent in the mechanical response of the samples tested at room temperature. In fact, microcracks nucleated at the surface together with the internal porosities appear to lead to the failure modes. It is well

Table 4 Tensile properties of Ti6242 alloys processed via different manufacturing technologies

Condition	YS [MPa]	UTS [MPa]	Elongation [%]	Ref.
As-built/EB-PBF	853 ± 10	914 ± 8	7.9 ± 0.9	This work
As-built/L-PBF	1293 ± 37	1381 ± 79	5.3	[18]
Cast + Aged	896	959	9	[37]
Cast + Solution + Aged	894	1010	8	[37]

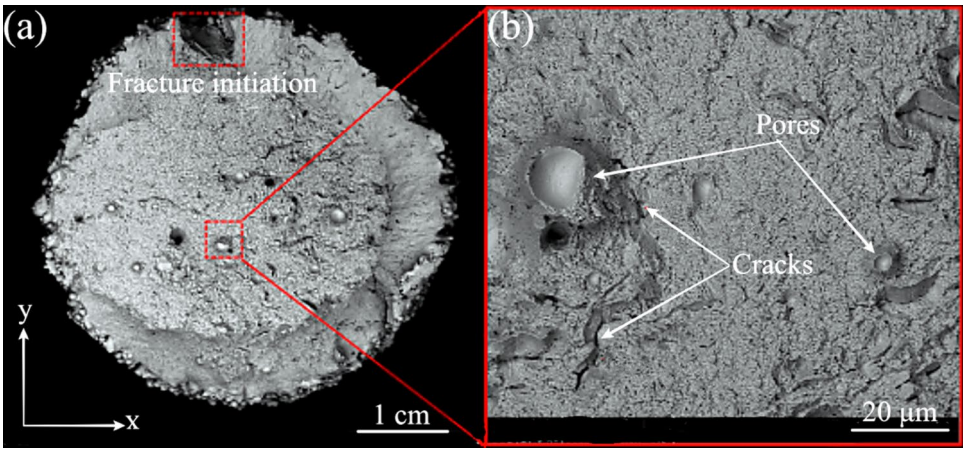

Fig. 8 Fracture surface of a Ti6242 sample tested at room temperature

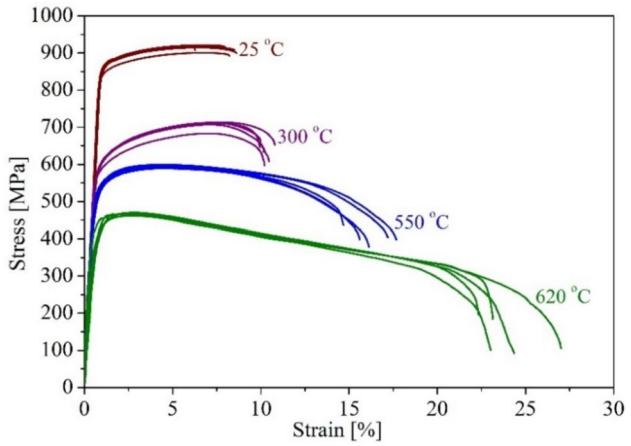

Fig. 9 Engineering tensile stress–strain curves of Ti6242 samples at 25, 300, 550, and 620 °C

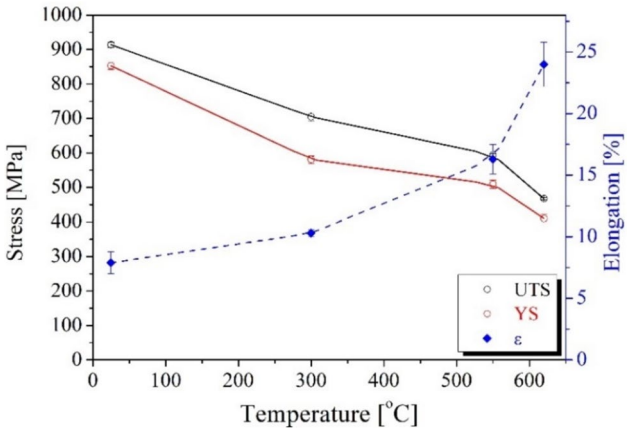

Fig. 10 YS, UTS, and ε of Ti6242 alloy as a function of test temperature

known that the surface roughness obtained by EB-PBF is much higher than that obtained by the *L*-PBF process. This difference is associated with several reasons, such as (i) the stronger staircase effect related to the higher layer thickness, (ii) the adhesion of the bigger partially melted powder to the outer surfaces, and (iii) the presence of open porosities on the outer surfaces (Fig. 8). It should be highlighted that the shape and surface of the internal porosities confirm that these porosities can be caused by the entrapped gas inside the starting powder. In fact, the presence of such a kind of defects inside the EB-PBF samples can act as stress concentration points under loading condition and increase the likelihood of crack initiation and consequently deteriorate the mechanical properties of materials. Figure 8 reveals that the fracture mode was a brittle–ductile fracture with a fibre zone in the centre and a shear slip peripheral area with an angle of 45° with respect to the BD.

Nevertheless, the results show that the EB-PBF process can be effectively used to produce high-ductility, complex-shaped Ti6242 parts with little compromise in tensile strength. Figure 9 compares the tensile stress–strain curves of the Ti6242 alloy produced by the EB-PBF process at room temperature with the curves at 300 °C, 550 °C, and 620 °C. As can be seen in the graph, results per temperature have high consistency with small deviation, confirming the homogeneity of the microstructure and robustness of the behaviour for all samples. All curves exhibit a strain-hardening behaviour and a necking point. The decrease in the flow stress after the yield stress at high temperatures (550 and 620 °C) can be explained by the contribution of dynamic and thermal softening mechanisms such as dynamic recovery and recrystallization.

The effect of test temperature on the UTS, YS, and ε of the Ti6242 alloy is plotted in Fig. 10. By increasing the tensile test temperature, the YS and UTS of the samples decreased from 914 and 853 MPa to 467 MPa and 410 MPa, while their elongation increased from 7.9% to 24%. As temperature increases, diffusion processes play a key role in the plastic deformation of the material and facilitate dislocation extinction at the same time as additional slip systems are activated, and consequently,

the Critical Resolved Shear Stress (CRSS) for plastic deformation of the material decreases [40, 41].

It is also well documented that raising the temperature facilitates dislocation extinction and migration and decreases dislocation density. This finding is in line with the XRD results [42]. Thus, when the temperature increases due to the facilitation of dislocation slip, the dislocation density decreases, as well as the dislocation multiplication rate, and consequently, the resistance of the material to plastic deformation decreases.

On the other hand, Hollomon's equation (Eq. 1) represents the relationship between the real stress, the strain-hardening coefficient and the strain-hardening index [43]

$$\mathrm{Log}\sigma_T = \mathrm{Log}K + n\mathrm{Log}\varepsilon_T, \tag{1}$$

where σ_T is the real stress, K is the strength coefficient, n is the strain-hardening index, and ε_T is the true strain.

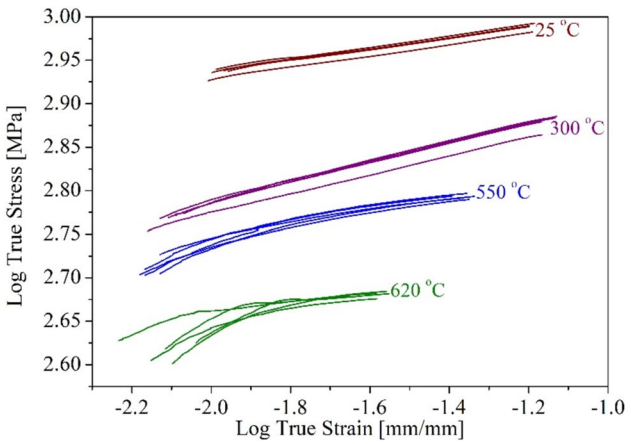

Fig. 11 The plot of Log true stress versus Log true strain for Ti6242 samples at different temperatures

According to this equation, the slope in the log true stress–log true strain plot is the strain-hardening index, and the strength coefficient can be calculated from the intercept of the curves (Fig. 11). In this work, the strain-hardening index and strength coefficient were calculated using the curves shown in Fig. 11. The results are provided in Fig. 12 and compared with the previous work and the alloy Ti64. As can be seen in this figure, when the temperature is increased from 25 °C to 620 °C, the strain-hardening index lies in the range of 0.06–0.11. It is interesting to point out that the variation of n and K for the samples processed in this work is in agreement with the results reported for Ti6242 [44]. Moreover, it should be highlighted that the higher strain-hardening index obtained for the EB-PBF Ti6242 samples compared to the Ti64 alloy confirms the higher temperature capability of the Ti6242 alloy. The better performance of the Ti6242 alloy can be attributed to the effect of the alloying elements, especially the interstitial ones. Indeed, Sn and Zr in the Ti6242 alloy are solid solution enhancers of α-Ti, and O and N as well-known interstitial elements that can strengthen the material [40]. The overall trend of n and K as a function of temperature also indicated that when the temperature increases, the resistance of the material to further deformation decreases. This means that the material can absorb more energy, and consequently, the fracture mechanism of the material changes from mixed mode to ductile mode. To evaluate this change in fracture mode, the fracture surface of the Ti6242 specimens shown in Fig. 13 was analysed.

Figure 13 shows the macroscopic fracture surface of alloy Ti6242 tested at room temperature, 300 °C, 550 °C, and 620 °C. Figure 13a shows a failure due to a brittle/ductile fracture with a fibre region and an obvious shear lip zone with an angle of 45° to the stress direction. It is well documented that the formation of a flat fracture zone is due to

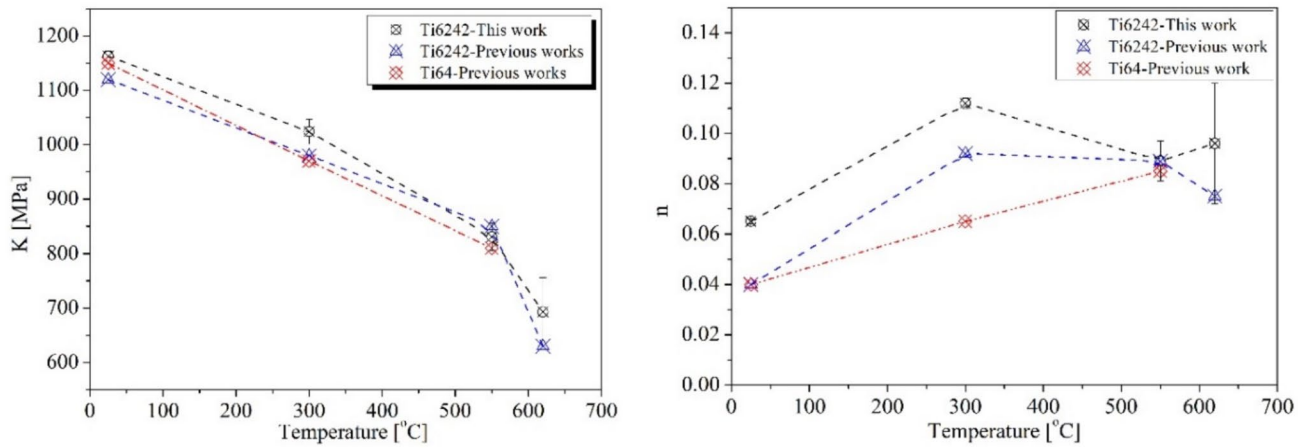

Fig. 12 Variation K and n as a function of temperature for Ti6242 and Ti64 alloy [44]

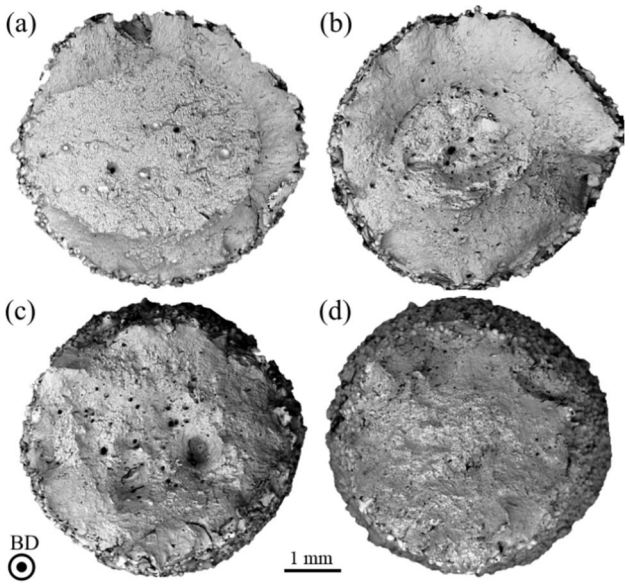

Fig. 13 Tensile rupture surface of Ti6242 sample at **a** 25 °C, **b** 300 °C, **c** 550 °C, and **d** 620 °C

plane strain conditions, while the formation of a slant fracture is due to plane stress conditions [45].

As can be seen in Fig. 13, the crack nucleated from a superficial defect that propagated afterwards and deteriorated the mechanical properties. As mentioned earlier, an increase in temperature increases the ductility of the material. This aspect can be clearly seen in the fracture surfaces, where the fibre zone increases with increasing temperature. This figure also shows that at high temperatures, there is no obvious fibre zone or shear lip area on the fracture surface of the specimens.

Figure 14 compares the fracture surface of the Ti6242 sample at 25 °C and 300 °C. As can be seen in Fig. 14a, b, the fracture initiation site located on the external surface of the samples confirms the important effect of the surface roughness on the mechanical properties of the metallic materials. Moreover, it is revealed that in the central part of the sample, some other defects, such as porosity and cracks, could significantly reduce the effective load-bearing capacity of the samples, leading to premature failure. Instead, Fig. 14c, d shows that even if, in this case, the failure started again from the surface defects, the fracture surface confirms that the ductility of the material slightly increased. Higher magnifications of the surfaces in Fig. 13 can be seen in Fig. 15 (for the central part) and Fig. 16 (for the surrounding part). A deeper analysis of the fibre zone (Figs. 14 and 15) confirms the presence of cleavage planes and dimples in the rupture surface at room temperature, which are typical of the mixed brittle and ductile fracture mode. However, the high-magnification

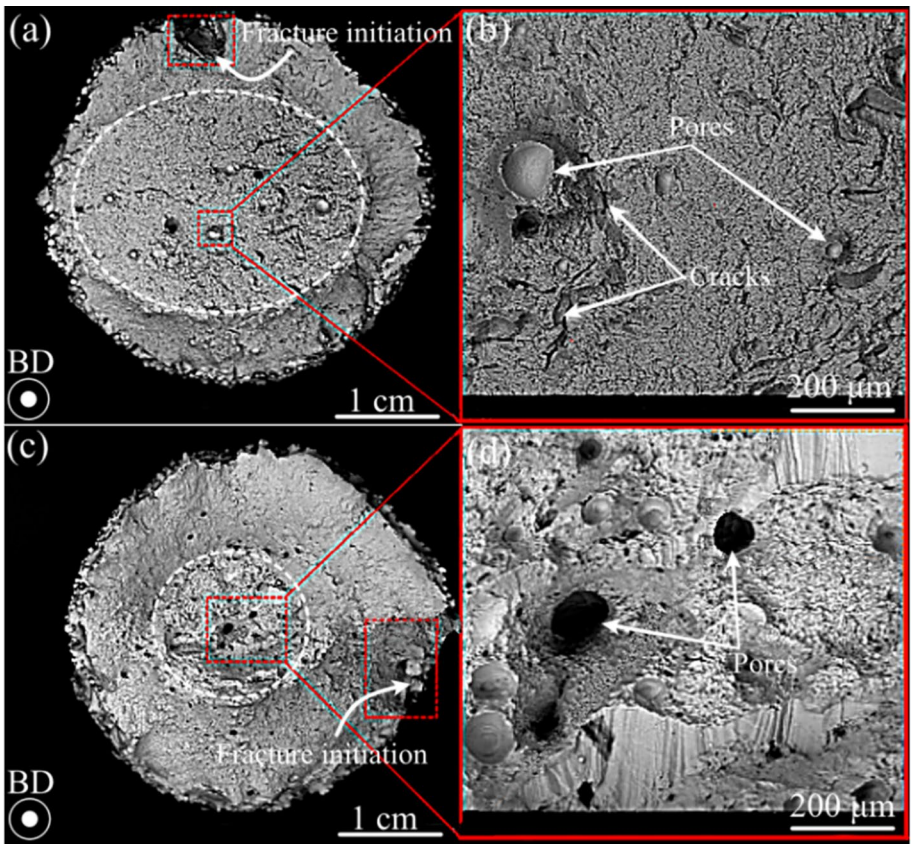

Fig. 14 Tensile rupture surface of Ti6242 sample at **a**, **b** 25 °C and **c**, **d** 300 °C

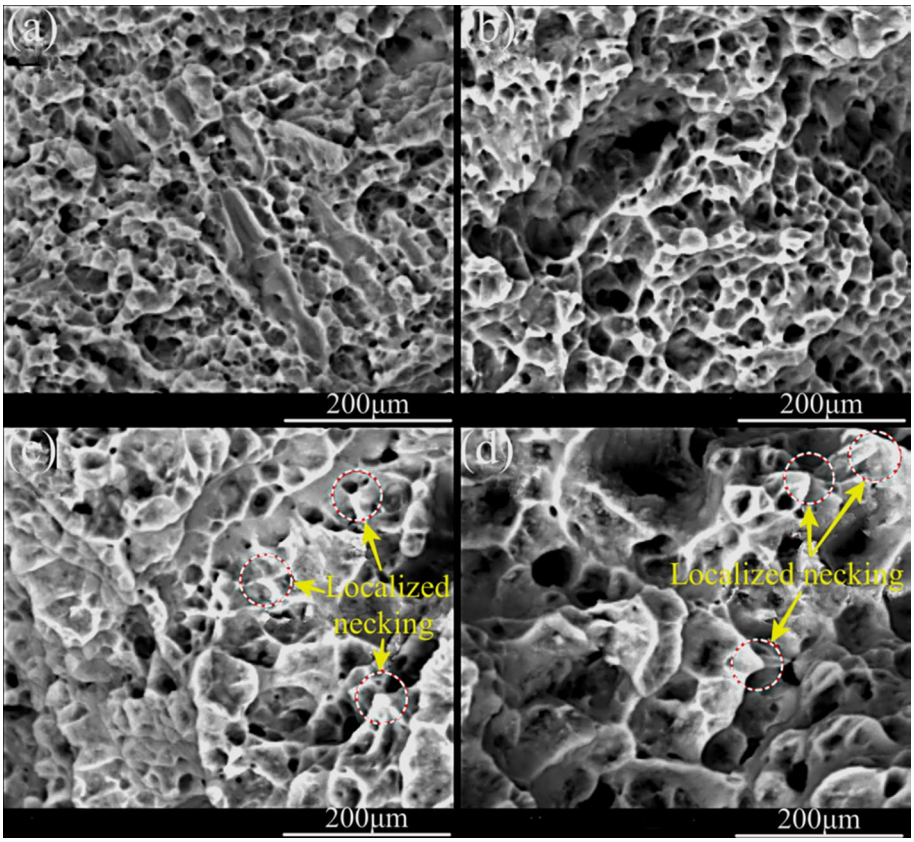

Fig. 15 Rupture surface of Ti6242 tensile samples in the central part: **a** room temperature, **b** 300 °C, **c** 550 °C, and **d** 620 °C

SEM micrographs of the Ti6242 specimens tested at high temperatures (550 °C and 620 °C) only display dimples, and no cleavage plane was found. This finding confirms the transition of the failure mode from mixed to ductile at high temperatures.

Figure 15 also shows that the fracture surface was uneven with increasing temperature, with typical cup, cone failure, and a higher proportion of necking. Also, as can be seen, the size and depth of dimples increased by raising the temperature. The increase in the size of the dimples as a function of temperature, which resulted in lower mechanical strength, is in good agreement with the microstructural observations. On the other hand, the formation of deeper dimples at high temperatures, confirming a higher plastic deformation capacity, could also be expected from the flow stress curves of the Ti6242 samples at elevated temperatures shown in Fig. 9. Figure 16 instead shows the rupture morphology of the samples from the region close to their outer surface. The fractography of this zone is also consistent with the deformability results mentioned above. The fracture surface in this zone consists of an uneven distribution of shallow dimples. The formation and this type of distribution of shallow dimples are considered to be a sign of low ductility in non-brittle materials. It is interesting to note that even in this zone, the size and depth of shallow dimples and the occurrence of localized necking sites increase as a function of temperature. This trend again confirms the change in ductility of the material due to an increase in working temperature.

4 Conclusions

This work aims to study the microstructural evolution and mechanical properties of EB-PBF Ti6242 at high temperatures. Hence, tensile tests were performed at 25 °C, 300 °C, 550 °C, and 620 °C with a constant strain rate and the correlation between the mechanical properties and microstructural evolution at elevated temperatures was investigated. The following conclusions can be drawn from this study.

- No cracks, macro-porosity, chemical inhomogeneities, or layer banding were observed in the as-built Ti6242 samples, confirming the successful processing of this alloy via the EB-PBF process.
- Microstructural observations confirmed epitaxial grain growth along the steep temperature gradient in the build direction, resulting in the formation of columnar β-grains with an average width of 30–60 µm. Within the prior β gains, a preliminary Widmanstätten microstructure with basket-weave morphology and α-colonies was revealed.
- When the test temperature was increased, there was no significant growth in the prior β grain size, while the

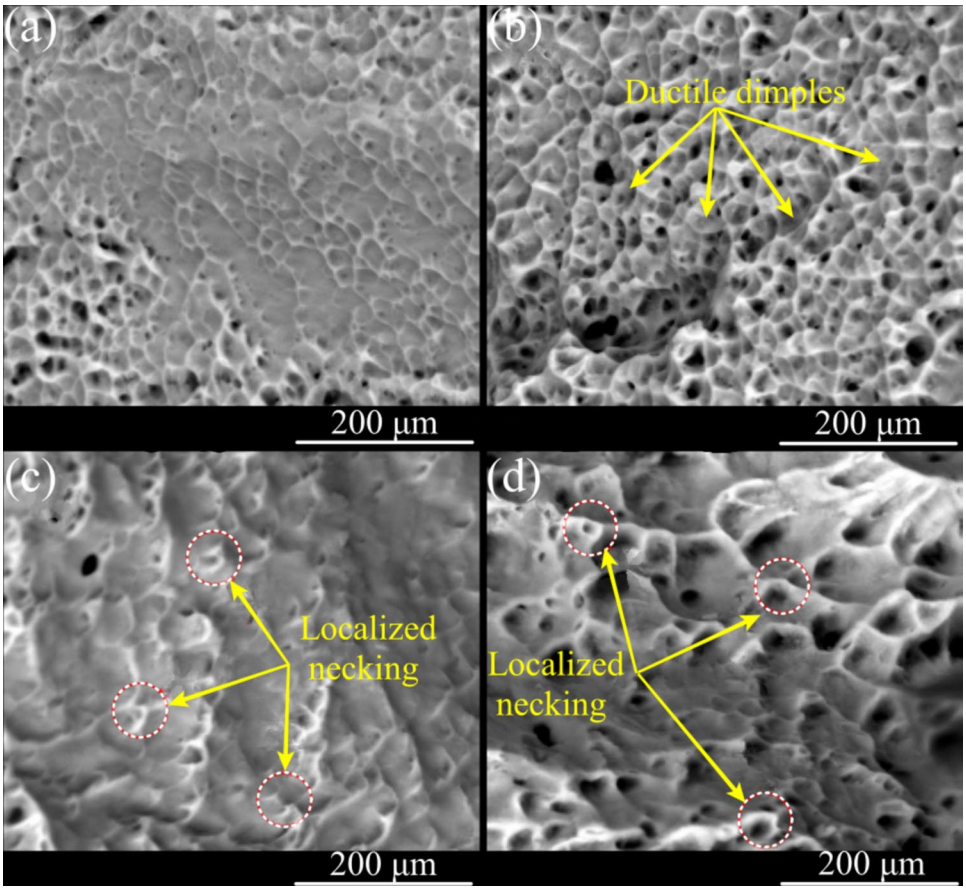

Fig. 16 Rupture surface of Ti6242 tensile samples from the slanted part: **a** room temperature, **b** 300 °C, **c** 550 °C, and **d** 620 °C

width of the α-lath increased from 0.75 µm at baseline to 0.92 µm, 1.11 µm, and 1.75 µm at 300 °C, 550 °C, and 620 °C, respectively. The average prior β grain width remains in the range of 30–60 µm, which corresponds to the range of the as-built samples.

- In contrast to the Ti6242 alloy processed via the *L*-PBF process, which is characterized by a complete α/α' phase, the samples from EB-PBF exhibited a duplex α-phase with hexagonal closed-packed structure and a β-phase with a body-centred cubic structure. In contrast to the thermodynamic calculations concerning the precipitation of silicide, no peak associated with this phase was found.
- With increasing temperature, the lattice strain decreased, while the crystallite size increased. Moreover, the variation of FWHM confirms that the dislocation density of Ti6242 samples decreased when the test temperature increased from room temperature to 620 °C, and consequently, the lattice parameter changed.
- The general overview of the flow curves shows that all samples exhibited strain-hardening behaviour up to the necking point with lower stress levels at higher temperatures. It is revealed that by increasing the tensile test temperature, the YS and UTS of the samples decreased from 914 and 853 MPa to 467 MPa and 410 MPa, while their elongation increased from 7.9% to 24%. By increasing the temperature from 25 °C to 620 °C, the strain-hardening index is in the range of 0.06–0.11.

Funding Open access funding provided by Politecnico di Torino within the CRUI-CARE Agreement.

Declarations

Conflict of interest No potential conflict of interest was reported by the authors.

References

1. Mosallanejad MH, Niroumand B, Aversa A, Manfredi D, Saboori A (2020) Laser powder bed fusion in-situ alloying of Ti-5%Cu alloy: process-structure relationships. J Alloys Compd. https://doi.org/10.1016/j.jallcom.2020.157558
2. Bandekhoda MR, Mosallanejad MH, Atapour M, Iuliano L, Saboori A (2024) Investigation on the potential of laser and electron beam additively manufactured Ti–6Al–4V components for orthopedic applications. Met Mater Int 30:114–126. https://doi.org/10.1007/s12540-023-01496-6
3. Prasad K, Karamched PS, Bhattacharjee A, Kumar V, Rao KBS, Sundararaman M (2015) Electron back scattered diffraction characterization of thermomechanical fatigue crack propagation of a near α titanium alloy Timetal 834. Mater Des 65:297–311
4. Zhang A, Liu D, Wang H (2013) Effect of thermal exposure on microstructure and tensile properties of laser deposited Ti60A alloy. Mater Sci Eng A 562:61–68
5. Banerjee D, Williams JC (2013) Perspectives on titanium science and technology. Acta Mater 61:844–879. https://doi.org/10.1016/j.actamat.2012.10.043
6. Niu Y, Li M (2009) Effect of 0.16 wt% hydrogen addition on high temperature deformation behavior of the Ti600 titanium alloy. Mater Sci Eng A 513:228–232
7. Yang L, Liu J, Tan J, Chen Z, Wang Q, Yang R (2014) Dwell and normal cyclic fatigue behaviours of Ti60 alloy. J Mater Sci Technol 30:706–709
8. Lopez M, Pickett C, Arrieta E, Murr LE, Wicker RB, Ahlfors M, Godfrey D, Medina F (2020) Effects of postprocess hot isostatic pressing treatments on the mechanical performance of EBM fabricated TI-6Al-2Sn-4Zr-2Mo. Materials (Basel). https://doi.org/10.3390/ma13112604
9. Perumal A, Azhagurajan A, Baskaran S, Prithivirajan R, Narayansamy P (2019) Statistical evaluation and performance analysis of electrical discharge machining (EDM) characteristics of hard Ti–6Al–2Sn–4Zr–2Mo alloy. Mater Res Express. https://doi.org/10.1088/2053-1591/ab06da
10. Galati M, Defanti S, Saboori A, Rizza G, Tognoli E, Vincenzi N, Gatto A, Iuliano L (2022) An investigation on the processing conditions of Ti–6Al–2Sn–4Zr–2Mo by electron beam powder bed fusion: microstructure, defect distribution, mechanical properties and dimensional accuracy. Addit Manuf 50:102564. https://doi.org/10.1016/j.addma.2021.102564
11. Yu Y, Hui S-X, Ye W-J, Wang X-Z, Zhang Z (2005) Effect of heat treatment process on the mechanical properties of Ti-Al-Sn-Zr-Mo-Si-X series alloys. Heat Treat Met 30:68–71
12. Peng W, Zeng W, Wang Q, Yu H (2013) Comparative study on constitutive relationship of as-cast Ti60 titanium alloy during hot deformation based on Arrhenius-type and artificial neural network models. Mater Des 51:95–104
13. Chamanfar A, Pasang T, Ventura A, Misiolek WZ (2016) Mechanical properties and microstructure of laser welded Ti–6Al–2Sn–4Zr–2Mo (Ti6242) titanium alloy. Mater Sci Eng A. https://doi.org/10.1016/j.msea.2016.02.068
14. Veiga C, Davim JP, Loureiro AJR (2012) Properties and applications of titanium alloys: a brief review. Rev Adv Mater Sci 32:133–148
15. Mosallanejad MH, Abdi A, Karpasand F, Nassiri N, Iuliano L, Saboori A (2023) Additive manufacturing of titanium alloys: processability, properties, and applications. Adv Eng Mater 25:2301122. https://doi.org/10.1002/adem.202301122
16. Mosallanejad MH, Abdi A, Karpasand F, Nassiri N, Iuliano L, Saboori A (2023) Additive manufacturing of titanium alloys: processability, properties, and applications. Adv Eng Mater. https://doi.org/10.1002/adem.202301122
17. Ghorbani HR, Mosallanejad MH, Atapour M, Galati M, Saboori A (2022) Hybrid additive manufacturing of an electron beam powder bed fused Ti6Al4V by transient liquid phase bonding. J Mater Res Technol. https://doi.org/10.1016/j.jmrt.2022.07.009
18. Vafaei M, Ghanavati R, Saboori A, Iuliano L (2024) The impact of heat treatment on microstructure, residual stress, and mechanical behavior of laser powder bed fusion additively manufactured Ti–6Al–2Sn–4Zr–2Mo alloy. J Mater Res Technol. https://doi.org/10.1016/j.jmrt.2024.10.202
19. Zhu Z, Ng FL, Seet HL, Nai SML (2022) Tailoring the microstructure and mechanical property of laser powder bed fusion fabricated Ti–6Al–2Sn–4Zr–2Mo via heat treatment. J Alloys Compd. https://doi.org/10.1016/j.jallcom.2021.162648
20. Fleißner-Rieger C, Pfeifer T, Jörg T, Kremmer T, Brabetz M, Clemens H, Mayer S (2021) Selective laser melting of a Near-α Ti6242S alloy for high-performance automotive parts. Adv Eng Mater 23:2001194. https://doi.org/10.1002/adem.202001194
21. Fujieda T, Cui Y, Aoyagi K, Koizumi Y, Chiba A (2018) Electron beam melting of boron-modified Ti–2Al–2Sn–4Zr–2Mo–0.1Si alloy with superior tensile strength and oxidation resistance at elevated temperatures. Materialia. https://doi.org/10.1016/j.mtla.2018.10.013
22. Cui Y, Aoyagi K, Koizumi Y, Fujieda T, Chiba A (2020) Enhanced oxidation resistance of a titanium–based alloy by the addition of boron and the application of electron beam melting. Addit Manuf. https://doi.org/10.1016/j.addma.2019.100971
23. Dharmendra C, Hadadzadeh A, Amirkhiz BS, Lloyd A, Mohammadi M (2020) Deformation mechanisms and fracture of electron beam melted Ti–6Al–4V. Mater Sci Eng A. https://doi.org/10.1016/j.msea.2019.138652
24. Raghavan S, Nai MLS, Wang P, Sin WJ, Li T, Wei J (2018) Heat treatment of electron beam melted (EBM) Ti-6Al-4V: microstructure to mechanical property correlations. Rapid Prototyp J 24:774–783. https://doi.org/10.1108/RPJ-05-2016-0070
25. Taghian M, Mani H, Mosallanejad M, Abdi A, Saboori A, Iuliano L (2024) Critical condition for initiation of dynamic recrystallisation in electron beam powder bed fused Ti-6Al-4 V Alloy. J Alloys Compd 1005:176165. https://doi.org/10.1016/j.jallcom.2024.176165
26. Davis AE, Caballero AE, Biswal R, Williams S, Prangnell PB (2022) Comparison of Microstructure Refinement in Wire-Arc Additively Manufactured Ti–6Al–2Sn–4Zr–2Mo–0.1Si and Ti–6Al–4V Built With Inter-Pass Deformation. Metall Mater Trans A 53:3833–3852. https://doi.org/10.1007/s11661-022-06811-1
27. Ackerman AK, Knowles AJ, Gardner HM, Németh AAN, Bantounas I, Radecka A, Moody MP, Bagot PAJ, Reed RC, Rugg D, Dye D (2020) The kinetics of primary alpha plate growth in titanium alloys. Metall Mater Trans A 51:131–141. https://doi.org/10.1007/s11661-019-05472-x
28. Cahn JW (1962) The impurity-drag effect in grain boundary motion. Acta Metall 10:789–798. https://doi.org/10.1016/0001-6160(62)90092-5
29. Radecka A, Coakley J, Vorontsov VA, Martin TL, Bagot PAJ, Moody MP, Rugg D, Dye D (2016) Precipitation of the ordered α2 phase in a near-α titanium alloy. Scr Mater 117:81–85. https://doi.org/10.1016/j.scriptamat.2016.02.015
30. Yue K, Liu J, Zhang H, Yu H, Song Y, Hu Q, Wang Q, Yang R (2020) Precipitates and alloying elements distribution in near α titanium alloy Ti65. J Mater Sci Technol 36:91–96. https://doi.org/10.1016/j.jmst.2019.03.018
31. Wang LM, Lin HC, Tsai CJ (2012) Characterization and mechanism of α2-Ti3Al and γ-TiAl precipitation in Ti-6Al-4V alloy following tungsten arc welding. Key Eng Mater 520:320–329. https://doi.org/10.4028/www.scientific.net/KEM.520.320

32. Köppers M, Herzig C, Friesel M, Mishin Y (1997) Intrinsic self-diffusion and substitutional Al diffusion in α-Ti. Acta Mater 45:4181–4191. https://doi.org/10.1016/S1359-6454(97)00078-5
33. Li J, Wang HM (2013) Aging response of laser melting deposited Ti–6Al–2Zr–1Mo–1V alloy. Mater Sci Eng A 560:193–199. https://doi.org/10.1016/j.msea.2012.09.055
34. Liang SX, Ma MZ, Jing R, Zhou YK, Jing Q, Liu RP (2012) Preparation of the ZrTiAlV alloy with ultra-high strength and good ductility. Mater Sci Eng A 539:42–47. https://doi.org/10.1016/j.msea.2012.01.022
35. Fultz B, Howe JM (2001) Diffraction and the X-Ray Powder Diffractometer. In: Transm. Electron Microsc. Diffractometry Mater, Springer Berlin Heidelberg, Berlin, Heidelberg, pp. 1–61. https://doi.org/10.1007/978-3-662-04516-9_1
36. Biju V, Sugathan N, Vrinda V, Salini SL (2008) Estimation of lattice strain in nanocrystalline silver from X-ray diffraction line broadening. J Mater Sci 43:1175–1179. https://doi.org/10.1007/s10853-007-2300-8
37. Welsch G, Boyer R, Collings EW (1993) Materials properties handbook: titanium alloys. ASM International
38. Mosallanejad MH, Niroumand B, Ghibaudo C, Biamino S, Salmi A, Fino P, Saboori A (2022) In-situ alloying of a fine grained fully equiaxed Ti-based alloy via electron beam powder bed fusion additive manufacturing process. Addit Manuf 56:102878. https://doi.org/10.1016/j.addma.2022.102878
39. AMS 4976 G, Titanium alloy, forgings 6.0Al–2.0Sn–4.0Zr–2.0Mo solution and precipitation heat–treated (SAE–AMS/MAM), 2008
40. Lütjering G, Williams JC (2007) Titanium matrix composites, Springer
41. Tanaka M, Hayashi Y, Okuyama Y, Morikawa T, Higashida K (2019) Change in Slip Mode with Temperature in Ti–0.49 mass% O. Mater Trans 60:80–85
42. Li P-H, Guo W-G, Huang W-D, Su Y, Lin X, Yuan K-B (2015) Thermomechanical response of 3D laser-deposited Ti–6Al–4V alloy over a wide range of strain rates and temperatures. Mater Sci Eng A 647:34–42
43. Gottstein G (2004) Physical foundations of materials science, Springer
44. Rajendran R, Venkateshwarlu M, Petley V, Verma S (2014) Strain hardening exponents and strength coefficients for aeroengine isotropic metallic materials—a reverse engineering approach. J Mech Behav Mater 23:101–106. https://doi.org/10.1515/jmbm-2014-0012
45. Qiu C, Wu X, Mei J, Andrews P, Voice W (2013) Influence of heat treatment on microstructure and tensile behavior of a hot isostatically pressed nickel-based superalloy. J Alloys Compd 578:454–464